# NON-IDEAL COMPRESSIBLE-FLUID DYNAMICS SIMULATIONS IN ORC TURBINES WITH A DISCONTINUOUS GALERKIN SOLVER

A. Colombo[1], A. Ghidoni[2], E. Mantecca[2], G. Noventa[2],
S. Rebay[2], D. Pasquale[3]

[1] University of Bergamo, Department of Engineering and Applied Sciences
viale Marconi 5, 24044 Dalmine (BG), Italy
e-mail: alessandro.colombo@unibg.it
[2] University of Brescia, Department of Mechanical and Industrial Engineering
via Branze 38, 25123 Brescia (BS), Italy
email: (antonio.ghidoni,e.mantecca,gianmaria.noventa,stefano.rebay)@unibs.it
[3] Turboden S.p.A.
via Cernaia 10, 25124 Brescia (BS), Italy
email: david.pasquale@turboden.it

## ABSTRACT

**This work aims to show the new capabilities implemented in an in-house discontinuous Galerkin solver for the numerical simulation of Organic Rankine Cycles turbine stages. The RANS equations coupled with a turbulence model are solved to predict the flow features in a multi reference frame, where interfaces between fixed and rotating zones are treated with a mixing plane approach and non-reflecting boundary conditions are used. The thermal pressure-explicit equation of state of Peng-Robinson is used to accurately relate thermodynamic quantities and is supplemented by a polynomial description of the ideal gas contribution to the isobaric specific heat. The solver is assessed with the computation of the flow field through the first stage of an existing axial ORC turbine provided by Turboden S.p.A..**

## KEYWORDS

DISCONTINUOUS GALERKIN, ORC, TURBINE, MIXING PLANE, REAL GAS, NON REFLECTING

## INTRODUCTION

Non-ideal compressible flows are nowadays widespread in many industrial fields. For example, the working fluid (heavy hydrocarbons, fluorocarbons and siloxanes) for an Organic Rankine Cycle (ORC) turbomachinery can show a non-ideal thermodynamic behaviour in the region where the expansion takes place, i.e., when pressure and temperatures are close to the liquid-vapour saturation curve in the region near the critical point.

1

Under these conditions, the ideal gas law fails in predicting accurately the thermodynamic behaviour of the fluid, and more complex equations of state (EoS) are required.

To enhance the design of this family of turbomachinery, in recent years the coupling of an accurate Computational Fluid Dynamics (CFD) with sophisticated thermodynamic models has been investigated, mainly for finite volume (FV) solvers (Pini et al., 2017). However, the increasing computational power and the higher accuracy expected by the design offices worldwide, motivate the recent interest in higher-order accurate solvers. In particular, discontinuous Galerkin (dG) methods are particularly attractive for their geometrical flexibility, simple implementation of $h/p$ adaptive algorithms (Bassi et al., 2020), and compact stencil. Their drawback with respect to standard FV solvers is the higher computation cost, which prevents a widespread application.

This work aims to show the capabilities of an in-house dG solver (Bassi et al., 2015) based on two different gas model, the polytropic ideal gas (PIG) and the Peng, Robinson (1976) (PR) EoS, for the numerical simulation of ORC turbines. The Reynolds averaged Navier-Stokes (RANS) equations coupled with the $k$-$\tilde{\omega}$ turbulence model are solved to predict the flow features in a multi-reference frame. The interfaces between fixed and rotating zones are treated with a mixing plane approach and non-reflecting boundary conditions (NRBC) (Saxer, Giles, 1993) are used. The thermal pressure-explicit EoS of Peng, Robinson (1976) is used to accurately relate thermodynamic quantities, and is supplemented by a polynomial description of the ideal gas contribution to the isobaric specific heat. The solver is assessed with the computation of the flow field through the first stage of an existing axial ORC turbine (2 stages) provided by Turboden S.p.A., with a comparison respect standard reflecting boundary conditions (RBC) and the ideal gas model. The knowledge gap of this work lies in the coupling of complex EoS for real gas, non-reflecting boundary conditions, and a mixing plane, in a high-order dG numerical framework for the discretization of RANS equations for turbulent flows. The proposed dG solver is, at least to authors knowledge, the first available in literature.

## 1  GOVERNING EQUATIONS

Using Einestein's notation, the RANS and $k$-$\tilde{\omega}$ turbulence model equations can be written for both fixed and rotating frames as

$$\frac{\partial \rho}{\partial t} + \frac{\partial}{\partial x_j}(\rho u_{r,j}) = 0, \tag{1}$$

$$\frac{\partial}{\partial t}(\rho u_i) + \frac{\partial}{\partial x_j}(\rho u_{r,j} u_i) = -\frac{\partial p}{\partial x_i} - \rho s_{r,i} + \frac{\partial \widehat{\tau}_{ji}}{\partial x_j}, \tag{2}$$

$$\frac{\partial}{\partial t}(\rho E) + \frac{\partial}{\partial x_j}(\rho u_{r,j} H) = \frac{\partial}{\partial x_j}\left[u_i \widehat{\tau}_{ij} - \widehat{q}_j\right] - \tau_{ij}\frac{\partial u_i}{\partial x_j} + \beta^* \rho \overline{k} e^{\widetilde{\omega}_r}, \tag{3}$$

$$\frac{\partial}{\partial t}(\rho k) + \frac{\partial}{\partial x_j}(\rho u_{r,j} k) = \frac{\partial}{\partial x_j}\left[(\mu + \sigma^* \overline{\mu}_t)\frac{\partial k}{\partial x_j}\right] + \tau_{ij}\frac{\partial u_i}{\partial x_j} - \beta^* \rho \overline{k} e^{\widetilde{\omega}_r}, \tag{4}$$

2

$$\frac{\partial}{\partial t}(\rho\widetilde{\omega}) + \frac{\partial}{\partial x_j}(\rho u_{r,j}\widetilde{\omega}) = \frac{\partial}{\partial x_j}\left[(\mu + \sigma\overline{\mu}_t)\frac{\partial\widetilde{\omega}}{\partial x_j}\right] + \frac{\alpha}{\overline{k}}\tau_{ij}\frac{\partial u_i}{\partial x_j} - \beta\rho e^{\widetilde{\omega}_r} + (\mu + \sigma\overline{\mu}_t)\frac{\partial\widetilde{\omega}}{\partial x_k}\frac{\partial\widetilde{\omega}}{\partial x_k},$$

$$(5)$$

where $\rho$ is the fluid's density, $p$ the pressure and $u_i$ is the $i$-th component of the velocity field. By defining the parameter $f_r$ such that $f_r = 0$ in a fixed frame and $f_r = 1$ in a rotating one, $u_i$ is distinguished in an absolute or relative velocity, $u_{a,i}$ or $u_{r,i}$, respectively. The mass-specific total energy and enthalpy are defined as

$$E = e + u_k u_k/2 - f_r(\epsilon_{ijk}\Omega_i r_{c,j})(\epsilon_{ijk}\Omega_i r_{c,j})/2, \tag{6}$$

$$H = h + u_k u_k/2 - f_r(\epsilon_{ijk}\Omega_i r_{c,j})(\epsilon_{ijk}\Omega_i r_{c,j})/2, \tag{7}$$

where $e$ and $h = e + p/\rho$ are the fluid internal energy and enthalpy per unit mass, while $\Omega_i$ is the $i$-th component of the angular velocity of the rotating frame. In Eqs. (6) and (7) the Levi-Civita tensor $\epsilon_{ijk}$ is also defined, as well as the distance from the rotation axis $r_c$. In Eqs. (2) to (5), the turbulent and the overall shear stress tensors ($\tau_{ij}$ and $\hat{\tau}_{ij}$, respectively) can be defined as

$$\tau_{ij} = 2\overline{\mu}_t\left[S_{ij} - \frac{1}{3}\frac{\partial u_k}{\partial x_k}\delta_{ij}\right] - \frac{2}{3}\rho\overline{k}\delta_{ij}, \quad \widehat{\tau}_{ij} = 2\mu\left[S_{ij} - \frac{1}{3}\frac{\partial u_k}{\partial x_k}\delta_{ij}\right] + \tau_{ij}, \tag{8}$$

where $S_{ij} = (\partial u_i/\partial x_j + \partial u_j/\partial x_i)/2$ is the mean strain rate tensor, $\delta_{ij}$ is Kronecker's delta and $\overline{\mu}_t = \alpha^*\rho\overline{k}e^{-\widetilde{\omega}_r}$ is the turbulent viscosity, computed through the limited turbulent kinetic energy $\overline{k} = \max(0, k)$ and the value $\tilde{\omega}_r$ of the specific dissipation rate $\tilde{\omega} = \log(\omega)$, which ensures the realizability condition for the turbulent stresses. This value is also used to compute the turbulent kinetic energy production term in Eq. (3) and the destruction term in Eqs. (4) and (5). In Eq. (3) the conductive heat flux $\hat{q}_j$ is $\widehat{q}_j = -(\mu/\text{Pr} + \overline{\mu}_t/\text{Pr}_t)c_p\partial T/\partial x_j$, where $Pr$ and $Pr_t$ are the laminar and turbulent Prandtl number, $c_p$ is the isobaric mass-specific heat capacity, and $T$ the temperature of the fluid. In Eq. (2) the source term components $s_{r,i}$ are added to take into account the effect of the Coriolis and the centripetal acceleration, $2\boldsymbol{\Omega} \times \hat{\mathbf{u}}$ and $\boldsymbol{\Omega} \times \boldsymbol{\Omega} \times \mathbf{r}_c$, respectively, and is defined as

$$\mathbf{s}_r = \begin{pmatrix} 2(\Omega_2\hat{u}_3 - \Omega_3\hat{u}_2) + \Omega_2(\Omega_1 r_{c,2} - \Omega_2 r_{c,1}) - \Omega_3(\Omega_3 r_{c,1} - \Omega_1 r_{c,3}) \\ 2(\Omega_3\hat{u}_1 - \Omega_1\hat{u}_3) + \Omega_3(\Omega_2 r_{c,3} - \Omega_3 r_{c,2}) - \Omega_1(\Omega_1 r_{c,2} - \Omega_2 r_{c,1}) \\ 2(\Omega_1\hat{u}_2 - \Omega_2\hat{u}_1) + \Omega_1(\Omega_3 r_{c,1} - \Omega_1 r_{c,3}) - \Omega_2(\Omega_2 r_{c,3} - \Omega_3 r_{c,2}) \end{pmatrix}, \tag{9}$$

where $\hat{\mathbf{u}} = \mathbf{u}_r + f_r(\boldsymbol{\Omega} \times \mathbf{r}_c)$. $\alpha$, $\alpha^*$, $\beta$, $\beta^*$, $\sigma$, $\sigma^*$ are the closure parameters of the $k - \omega$ Wilcox turbulence model. Equations (1)-(5) can then be written in the following compact form as

$$\mathbf{P}(\mathbf{w})\frac{\partial\mathbf{w}}{\partial t} + \nabla \cdot \mathbf{F}_c(\mathbf{w}) + \nabla \cdot \mathbf{F}_v(\mathbf{w}, \nabla\mathbf{w}) + \mathbf{s}(\mathbf{w}, \nabla\mathbf{w}) = \mathbf{0}, \tag{10}$$

3

where $\mathbf{w}$ is the vector of the unknown variables, $\mathbf{F}_c$ and $\mathbf{F}_v$ are the convective and the viscous flux, respectively, while $\mathbf{s}$ is the vector of the source terms. The matrix $\mathbf{P}(\mathbf{w})$ is generated by the change of variables from the conservative to the primitive set $\mathbf{w} = \left[\widetilde{p}, u_1, u_2, u_3, \widetilde{T}, k, \widetilde{\omega}\right]^T$, where $\widetilde{p} = \log(p)$ and $\widetilde{T} = \log(T)$ are used to enhance the solver's robustness (Bassi et al., 2015).

## 2   THERMODYNAMIC MODELS AND TRANSPORT PROPERTIES

In this work, the thermodynamic properties of the working fluid are calculated with different gas model: the polytropic ideal gas (PIG) and the Peng, Robinson (1976) (PR) EoS. The simplest one is the PIG EoS, i.e., $p(\rho, T) = \rho R^* T$, where $R^* = \mathcal{R}/M_m$ is the specific gas constant, $\mathcal{R} = 8314 \; J/(mol \; K)$ the universal constant, and $M_m$ the molecular weight of the gas. For this model, Mayer's relation holds, hence the ideal gas isochoric specific heat $c_v^0$ is calculated as $c_v^0 = c_p^0 - R^*$, where $c_p^0(T) = \lim_{\rho \to 0} c_p(\rho, T)$ is the ideal gas isobaric specific heat and often given in the form of a polynomial of the absolute temperature. In this work, the form $c_{p,0}(T) = c_0 + c_1 T + c_2 T^2 + c_3 T^3$ is used, where the coefficients $c_i$ for $i = 0, \ldots, 3$ are treated as input data coming from functional fittings of experimental data or from chemical group contribution methods such as the ones in Poling et al. (2000). Polytropic behaviour is granted by choosing a constant reference value for $c_p^0$, marked as $c_{p,ref}^0$. Due to the operating conditions, this value is set at the critical temperature of the fluid $T_{cr}$, therefore we have a corresponding reference ideal gas isochoric specific heat $c_{v,ref}^0$ defined as $c_{v,ref}^0 = c_{p,ref}^0 - R^* = c_p^0(T_{cr}) - R^*$.

The Peng, Robinson (1976) EoS is given by

$$p(\rho, T) = \frac{\rho R^* T}{1 - \rho b} - \frac{a \rho^2 \phi^2(T)}{1 + 2\rho b - \rho^2 b^2}. \tag{11}$$

In Eq. (11), the terms $a$ and $b$ are constant parameters, which represent the intermolecular interaction between gas particles and their molecular volume respectively. They are functions of the fluid critical pressure and temperature $p_{cr}$ and $T_{cr}$, and they are calculated as $a = 0.45724 \left(R^* T_{cr}\right)^2 / p_{cr}$ and $b = 0.07780 R^* T_{cr} / p_{cr}$. The other parameter $\phi(T)$ is a temperature dependent quantity, and is calculated as $\phi(T) = 1 + \chi(1 - \sqrt{T/T_{cr}})$. In its expression, $\chi$ is a polynomial function of the acentric factor $\theta$, which accounts for the effects relative to molecular shape. In particular, it is defined as $\theta = -(1 + \log_{10}(p_{sat}/p_{cr})_{|T/T_{cr}=0.7})$, where $p_{sat}(T)$ is the saturation pressure of the fluid. It is a measure of the non sphericity of the fluid molecules and once its value is known, $\chi$ takes the form $\chi = 0.37464 + 1.54226\theta - 0.26992\theta^2$.

Following Reynolds (1979), the real gas mass-specific internal energy $e$ and entropy $s$ can be defined starting from any thermal EoS in the form $p = p(\rho, T)$. Their expres-

sions become

$$e(\rho, T) = e_0 + \int_{T_0}^{T} c_v^0(\eta) d\eta + \int_0^{\rho} \frac{1}{\xi^2} \left[ p - T \left( \frac{\partial p}{\partial T} \right)_\xi \right] d\xi, \qquad (12)$$

$$s(\rho, T) = s_0 + \int_{T_0}^{T} \frac{c_v^0(\eta)}{\eta} d\eta - R^* \log \left( \frac{\rho}{\rho_0} \right) + \int_0^{\rho} \frac{1}{\xi^2} \left[ \xi R^* - \left( \frac{\partial p}{\partial T} \right)_\xi \right] d\xi \qquad (13)$$

where $\xi$ and $\eta$ are used as symbolic substitutes of $\rho$ and $T$ in the integral functions and $(\rho_0, T_0)$ identifies an arbitrary reference state. The last integral in both Eq. (12) and Eq. (13) represent a deviation from the ideal gas behaviour, which is null for the PIG EoS. The real gas isochoric and isobaric specific heat are calculated as $c_v(\rho, T) = (\partial e / \partial T)_\rho$ and $c_p(\rho, T) = c_v + [T(\partial p / \partial T)_\rho^2]/[\rho^2(\partial p / \partial \rho)_T]$, using the general relations from Hanimann et al. (2020), while the speed of sound $c$ takes the form $c(\rho, T) = \sqrt{(c_p/c_v)(\partial p/\partial \rho)_T}$. The molecular dynamic viscosity $\mu$ is computed with a power law that approximates its variation with the temperature as $\mu(T) = \mu_{ref} (T/T_0)^{a_\mu}$, where $\mu_{ref}$ and $T_0$ are reference values, and the exponent $a_\mu$ is a constant parameter. By assuming a constant Prandtl number $Pr$, the molecular thermal conductivity $\lambda$ can be computed from the viscosity as $\lambda(\rho, T) = \mu c_p(\rho, T)/Pr$.

## 3 DISCONTINUOUS GALERKIN SOLVER

A short description of the discontinuous Galerkin discretization, from both the spatial (Sec. 3.1) and temporal (Sec. 3.2) point of view, is here reported. For an in-depth description see Bassi et al. (2015).

### 3.1 dG spatial discretization

Let $V = \{v \in L^2(\Omega) \mid \nabla v \in L^2(\Omega)\}$ be a space containing an infinite number of sufficiently smooth test functions $v$ and let $\Omega$ be a smooth physical domain. Let then $\partial\Omega$ be the frontier of $\Omega$ and $\mathbf{n}$ its outward pointing unit normal vector. The continuous semi-discrete variational weak formulation of the RANS equations over $\Omega$ is obtained after multiplying Eq. (10) by every $v \in V$ and integrating by parts the results over $\Omega$. A tringulation $\mathcal{T}_h$ of an approxmation $\Omega_h$ of $\Omega$ in $n_e$ non-overlapping elements is then given, with the correspondent set of faces $\mathcal{F}_h = \mathcal{F}_b \cup \mathcal{F}_i$ containing all the boundary ($\mathcal{F}_b$) and internal ($\mathcal{F}_b$) faces. An approximation of $V$ with the truncated space of polynomial functions of maximum degree $d$ in $n_d$ spatial dimensions is then made $\forall K \in \mathcal{T}_h$ as $V_h = \{v_h \in \mathbb{P}_{n_d}^d(K)\}$.

In particular, $V_h$ is chosen here as the set of orthonormal and hierarchical basis functions defined in each element from its principal inertial axes. For $j = 1, ..., n_u$ and $l = 1, ..., N_{dof}$, with $n_u = n_d + 4$ being the total number of unknowns and $N_{dof}$ the total number of basis functions in the element $K$, the discrete elemental solutions $\mathbf{w}_h$ are given by convex combinations of the basis functions as $w_{h,j}(\mathbf{x}, t) = W_{jl}(t)v_{h,l}(\mathbf{x})$,

5

where $W_{jl}(t)$ are the degrees of freedom of the solution in the element $K$ and $\mathbf{w}_h \in V_h$. The dG spatial discretization is obtained by writing the semi-discrete variational weak formulation of Eq. (10) $\forall K \in \mathcal{T}_h$, where $V$ and $\mathbf{w}$ are substituted by their discrete counterparts. A summation over all the elements is then performed, therefore, the complete semi-discrete problem consists in seek, for $i = 1, ..., N_{dof}$, for $m = 1, ..., n_u$ and for $n = 1, ..., n_d$, the elements of $\mathbf{W} \in \mathbb{R}^{n_u \times N_{dof} \times n_e}$ such that

$$
\sum_{K \in \mathcal{T}_h} \int_K v_{h,i} P_{jm}\left(\mathbf{w}_h\right) v_{h,l} \frac{dW_{jl}}{dt} d\mathbf{x} - \sum_{K \in \mathcal{T}_h} \int_K \frac{\partial v_{h,i}}{\partial x_n} F_{jn}\left(\mathbf{w}_h, \nabla \mathbf{w}_h + \mathbf{r}\left(\llbracket \mathbf{w}_h \rrbracket\right)\right) d\mathbf{x}
$$
$$
+ \sum_{K \in \mathcal{T}_h} \oint_{\partial K} \llbracket v_{h,i} \rrbracket \widehat{F}_j\left(\mathbf{w}_h^{\pm}, (\nabla \mathbf{w}_h + \eta \mathbf{r}_L\left(\llbracket \mathbf{w}_h \rrbracket\right))^{\pm}\right) d\sigma
$$
$$
+ \sum_{K \in \mathcal{T}_h} \int_K v_{h,i} s_j\left(\mathbf{w}_h, \nabla \mathbf{w}_h + \mathbf{r}\left(\llbracket \mathbf{w}_h \rrbracket\right)\right) d\mathbf{x} = 0.
$$
$$(14)$$

In this equation, $\mathbf{F} = \mathbf{F}_c + \mathbf{F}_v \in \mathbb{R}^{n_u} \times \mathbb{R}^{n_d}$ is the sum of the convective and viscous flux, while $\hat{\mathbf{F}} \in \mathbb{R}^{n_u}$ is a numerical flux function. In fact, since the dG method does not enforce the continuity of the solution across elements interfaces, a stable and consistent discretization is guaranteed only with the substitution of $\mathbf{F}$ with $\hat{\mathbf{F}}$ in the interface integrals. In this work, the convective part of $\hat{\mathbf{F}}$ is based on the solution of local Riemann problems with the approximate Riemann solver of Roe (1981), generalized to the case of an arbitrary EoS following the approach of Vinokur, Montagné (1990). The viscous part is instead discretized with the BR2 scheme (Bassi et al., 1997), by employing both local and global lifting operators $\mathbf{r}_L(\cdot)$ and $\mathbf{r}(\cdot)$ on the solution componentwise jump $\llbracket \mathbf{w}_h \rrbracket = \mathbf{w}_h^- \mathbf{n}^- + \mathbf{w}_h^+ \mathbf{n}^+$ across mesh faces. In this notation, $\mathbf{n}^-$ and $\mathbf{n}^+$ are the inward and outward pointing unit normal vectors to a face of an element $K$, respectively, while $\eta$ is the stability parameter of Arnold et al. (2002).

An artificial diffusion contribution is introduced inside each element according to the shock-capturing approach of Bassi et al. (2016), with a shock sensor function to detect discontinuities. In particular, the shock-capturing term is always and everywhere active in $\Omega_h$, but a numerical viscosity is introduced only in regions with nonphysical oscillations.

### 3.2 Time integration

After a numerical computation of the integrals in Eq. (14) with gaussian quadrature rules, the following system of ordinary differential equations (ODEs) in time is obtained

$$
\mathbf{M_P}\left(\mathbf{W}\right) \frac{d\mathbf{W}}{dt} + \mathbf{R}\left(\mathbf{W}\right) = \mathbf{0}, \tag{15}
$$

where $\mathbf{R}\left(\mathbf{W}\right)$ is the vector of the global residuals and $\mathbf{M_P}\left(\mathbf{W}\right)$ is the global block diagonal mass matrix which comes from the calculation of the first integral in Eq. (14).

The time integration of Eq. (15) is done with the Linearized Backward Euler (LBE) scheme, which can be written as

$$\left[\frac{\mathbf{M_P}\left(\mathbf{W}^n\right)}{\Delta t} + \frac{\partial \mathbf{R}\left(\mathbf{W}^n\right)}{\partial \mathbf{W}}\right]\left(\mathbf{W}^{n+1} - \mathbf{W}^n\right) = -\mathbf{R}\left(\mathbf{W}^n\right). \qquad (16)$$

For stationary problems, the pseudo-transient continuation strategy adopted in Bassi et al. (2014) is used. In this case, an exponential "CFL law" allows for progressively higher values of $\Delta t$. Since Eq. (16) represents an algebraic nonlinear system, an iterative method is required at every $n$. The linear systems which come from these inner iteration are solved using the restarted GMRES algorithm with an additive Schwarz preconditioner, as available in the PETSc library (pet, 2018).

### 3.3 Non-reflecting boundary conditions

A multi reference frame approach is implemented to treat the fixed (stator) and rotating (rotor) zones in a steady manner; these zones are coupled with a mixing plane approach and non-reflecting boundary conditions (Saxer, Giles, 1993) are used. The mixing-plane interface removes the dependency of the results on the relative position between the rotor and the stator. Outlet (upstream domain) and inlet (downstream domain) are averaged in the pitch-wise direction, and mixed-out average is used to guarantee the conservation of mass, momentum and energy.

In turbomachinery applications both the outflow and inflow boundary conditions are very close to the blades, and a small space exists between rotor and stator rows. Standard inflow/outflow boundary conditions lead to the appearance of fictitious reflections that compromise the accuracy of the solution. A set of boundary conditions that correctly describes the incoming waves is thus required to avoid spurious oscillations of the solution.

Saxer, Giles (1993) non reflecting boundary conditions (NRBC) are implemented in the solver. They assume that the solution at the boundary is circumferentially decomposed into Fourier modes, where the $0^{th}$ mode corresponds to the average solution. The average mode is treated according to standard one-dimensional characteristic theory that allows to specify physical or mixing plane quantities at the boundaries. The remaining part of the solution, i.e., the sum of the harmonics, is treated following the exact two dimensional theory proposed by Saxer, Giles (1993), The original two-dimensional theory can be extended to 3d by decoupling the tangential and the radial flow variation. In particular, the 2d approach is applied in the tangential direction on bands of constant span and quasi-three-dimensional behaviour is achieved by incorporating a radial equilibrium. Figure 1 (left) demonstrates the effectiveness of the implemented approach, as spurious reflections are suppressed. Moreover, Fig. 1 (right) shows also the pitchwise pressure distribution, $p/p_{01}$ on the outflow section at midspan. As expected, huge differences are evident for the use of RBC and NRBC boundary conditions. The effect of the EoS on the results is smaller and differences are confined in the wake region.
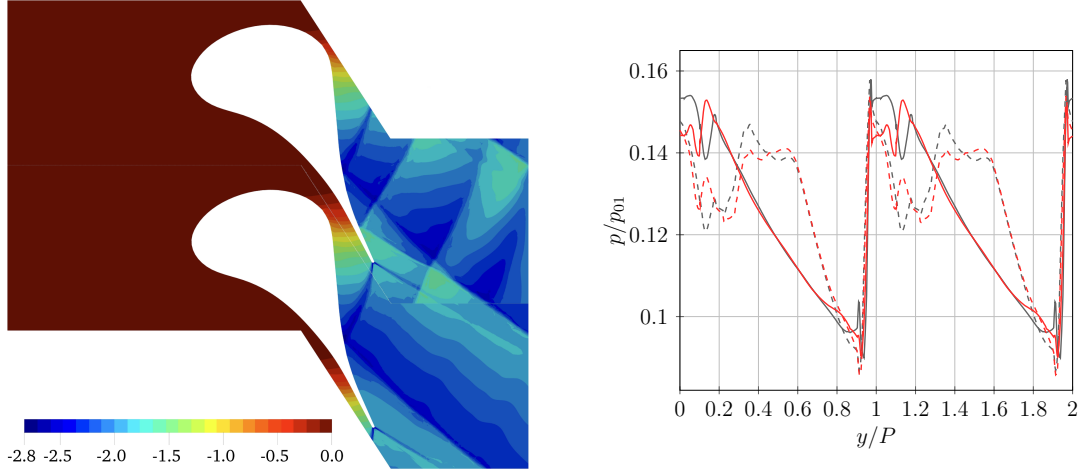
7

Figure 1: ORC nozzle. Contours of $\log(p/p_{01})$ with RBC (left, top blade) and NRBC (left, bottom blade) with PR EoS and $p/p_{01}$ pitchwise plot at outflow midspan for PIG and PR EoS (right). $dG - \mathbb{P}^2$ solution approximation. - - - PIG RBC, —— PIG NRBC, - - - PR RBC, —— PR NRBC. Distorted geometries: blade design is confidential property of the manufacturer.

## 4   RESULTS

The solver is used to investigate the real gas flow for a sub-critical expansion through the $i$) nozzle and the $ii$) first stage of an ORC turbine. The linear siloxane MDM ($C_8H_{24}O_2Si_3$) is the working fluid, having molecular weight $M_m = 236.531\ g/mol$, critical pressure $p_{cr} = 1.415 MPa$, critical temperature $T_{cr} = 564.09\ K$, and acentric factor $\theta = 0.5281$. The parameters used for the viscosity power law are $T_0 = T_{cr}$, $\mu_{ref} = 1.161 \times 10^{-5}\ Pa \cdot s$, and $a_\mu = 3/4$. For $c_p^0$ instead, the coefficients are $c_0 = 330.6\ J/(kg \cdot K)$, $c_1 = 4.236\ J/(kg \cdot K^2)$, $c_2 = -2.391 \times 10^{-3}\ J/(kg \cdot K^3)$, $c_3 = 5.546 \times 10^{-7}\ J/(kg \cdot K^4)$. A $\mathbb{P}^2$ solution approximation is used for the simulations with both the thermodynamic models, and the $L^2$ euclidean norm of all residuals ($||\mathbf{R}_i||_{L^2} < 10^{-9}$, $i = 1, \ldots, 7$) is used to check the convergence. The mesh of the nozzle has $5\,128$ quadratic elements, hexahedra in the boundary layer and prisms outside. The height of elements adjacent to the solid wall corresponds to a $y^+ \approx 5$. At the inflow, the total pressure, $p_{01} = 8\ bar$, total temperature, $T_{01} = 545\ K$, flow angle, $\alpha_1 = 0°$, turbulence intensity, $Tu_1 = 4\%$, and viscosity ratio, $(\mu_t/\mu)_1 = 10$, are set. While at the outflow, the static pressure is set equal to $p_2 = 1.33\ bar$. Figure 3 shows the convergence history for the simulation with NRBC and PR EoS. The results are compared with Colonna et al. (2008), where an inviscid high resolution finite volume solver and the state-of-art multi-parameter Helmholtz-explicit EoS is used. In particular, Fig. 4 shows the blade distribution for the pressure coefficient $C_p = (p_{01} - p)/(p_{01} - p_2)$, the density and the speed of sound. Despite the behaviour of $C_p$ is similar for all models,
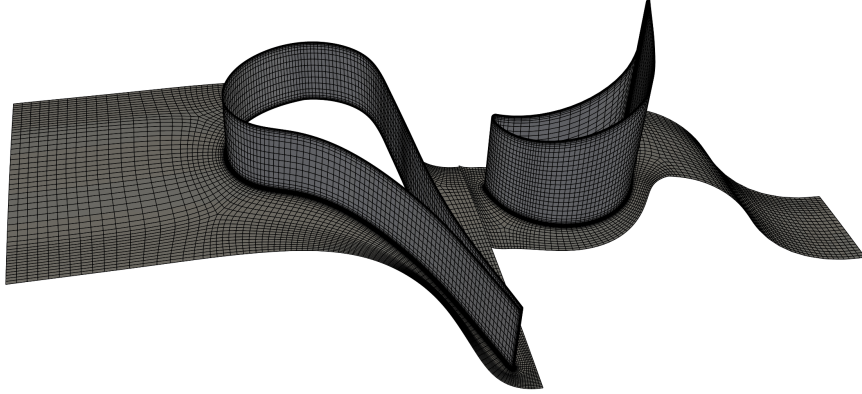
8

Figure 2: ORC turbine. Detail of the surface mesh of the $1^{st}$-stage.

the PIG EoS fails to predict reliable values of the other thermodynamic properties, especially the speed of sound, which is a crucial parameter in the fluid-dynamic simulation. This is due to the fact that the flow field in the nozzle is almost isothermal and the PIG EoS does not consider a dependence of $c$ from the density, that varies greatly through the expansion. The PR EoS shows instead a satisfactory qualitative and quantitative behaviour with respect to the model of Colonna et al. (2008). The maximum difference in the magnitude of the collected data is everywhere below $2.8\%$, and the other small differences, especially after the blade's trailing edge, are ascribed to the turbulent flow regime considered in these simulations.

For the complete first stage the mesh has $40\,080$ quadratic hexahedra, and the height of elements adjacent to the solid wall corresponds to a $y^+ \approx 5$ (see Fig. 2). At the inflow, the total pressure, $p_{01} = 9.57\ bar$, total temperature, $T_{01} = 535\ K$, flow angle, $\alpha_1 = 0°$, turbulence intensity, $Tu_1 = 4\%$, and viscosity ratio, $(\mu_t/\mu)_1 = 10$, are set. At the outflow, the static pressure is set equal to $p_2 = 1.17\ bar$, and the rotational speed of the rotor is set equal to $\mathbf{\Omega} = [0, 0, 314.16]^T\ rad/s$. Figure 5 shows the Mach number and the compressibility factor $z = p/(\rho R^* T)$ contours. In particular, the trailing edge shock impinges on the suction side of the adjacent blade, creating a small detachment of the boundary layer, and is reflected toward the stator outlet. As expected, spurious reflections are avoided. A small shock appears also through the rotor passage, which promotes a large separation. Real gas effects are confined in the first half of the stator, as pointed out by the low value of $z$ at the inlet. Ideal gas behaviour is fully recovered in the rotor.

**CONCLUSIONS**

In this work a discontineous Galerkin solver extended to the solution of turbomachinery stages, is used to investigate the expansion from subcritical inlet conditions through an ORC turbine nozzle and stage. The simulations are performed with the PIG
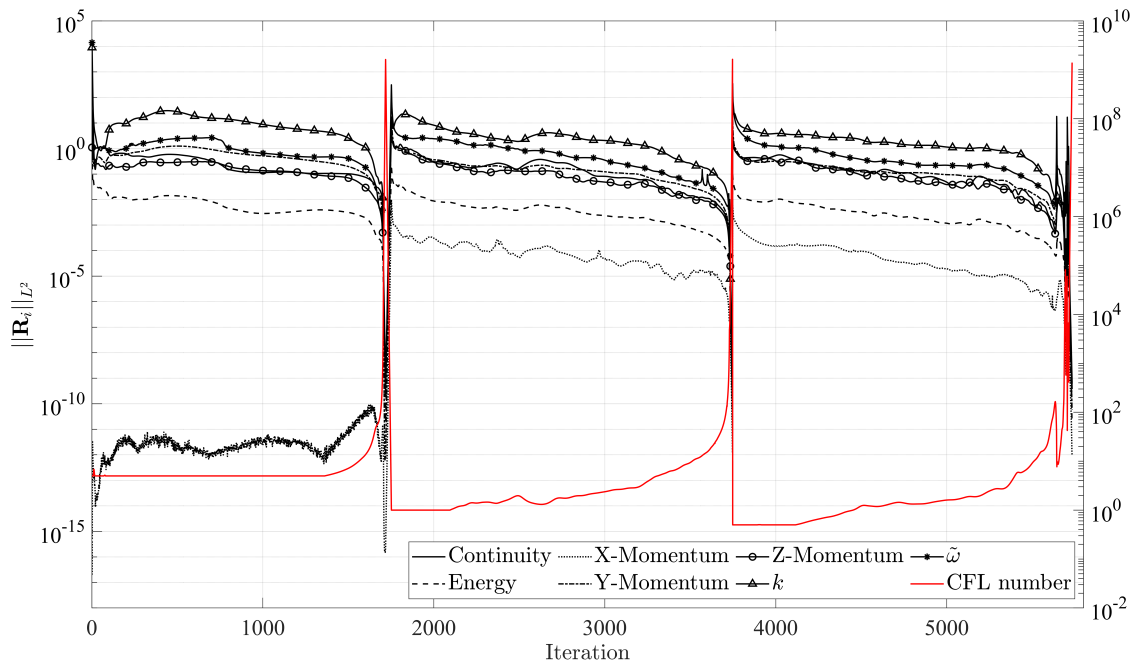
Figure 3: ORC nozzle. Convergence history using NRBC and PR EoS, $\mathbb{P}^{0\to 2}$ solution approximations.

and PR EoS, and non reflecting boundary conditions are used in a multiple reference frame approach. The stator-rotor coupling avoids nonphysical oscillations, also in a high order context. The use of a real gas model is mandatory in the first part of the expansion, where the PIG model provides wrong predictions.

Future work will be devoted to the implementation in the code of more complex thermodynamic and transport properties models, and to the assessment of the solver on more complex three-dimensional configurations.

## ACKNOWLEDGEMENTS

## REFERENCES

PETSc Web page. 2018.

*Arnold Douglas N., Brezzi Franco, Cockburn Bernardo, Marini L. Donatella.* Unified Analysis of Discontinuous Galerkin Methods for Elliptic Problems // SIAM Journal on Numerical Analysis. 2002. 39, 5. 1749–1779.

*Bassi F., Botti L., Colombo A., Crivellini A., De Bartolo C., Franchina N., Ghidoni A., Rebay S.* Time Integration in the Discontinuous Galerkin Code MIGALE - Steady
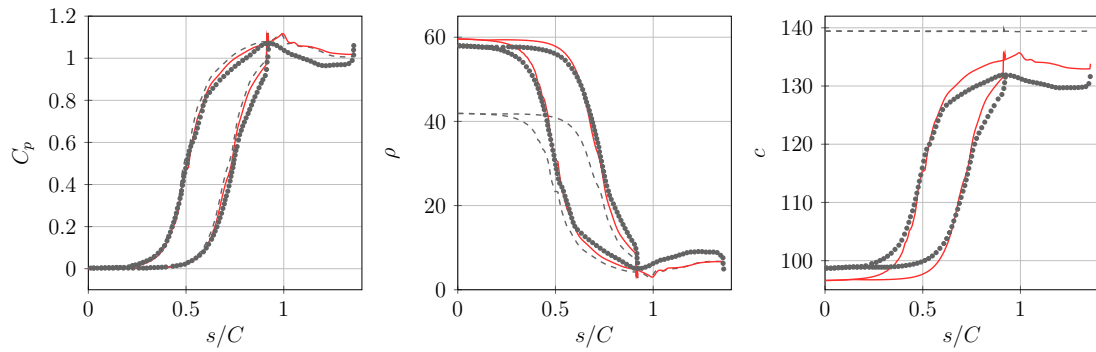
Figure 4: ORC nozzle. Pressure coefficient $C_p$, density $\rho\ [kg/m^3]$, and speed of sound $c\ [m/s]$ distributions along the blade profile. $\cdot$ Colonna et al. (2008) 2D inviscid, - - - $dG - \mathbb{P}^2$ RANS PIG, —— $dG - \mathbb{P}^2$ RANS PR.

Problems // IDIHOM: Industrialization of High-Order Methods - A Top-Down Approach: Results of a Collaborative Research Project Funded by the European Union, 2010 - 2014. Cham: Springer International Publishing, 2015. 179–204.

*Bassi F., Botti L., Colombo A., Crivellini A., Franchina N., Ghidoni A.* Assessment of a high-order accurate Discontinuous Galerkin method for turbomachinery flows // International Journal of Computational Fluid Dynamics. 2016. 30, 4. 307–328.

*Bassi F., Colombo A., Crivellini A., Fidkowski K.J., Franciolini M., Ghidoni A., Noventa G.* Entropy-Adjoint $p$-Adaptive Discontinuous Galerkin Method for the Under-Resolved Simulation of Turbulent Flows // AIAA Journal. 2020. 58, 9. 3963–3977.

*Bassi F., Ghidoni A., Perbellini A., Rebay S., Crivellini A., Franchina N., Savini M.* A high-order Discontinuous Galerkin solver for the incompressible RANS and $k - \omega$ turbulence model equations // Computers & Fluids. 2014. 98. 54–68.

*Bassi F., Rebay S., Mariotti G., Pedinotti S., Savini M.* A high-order accurate discontinuous finite element method for inviscid and viscous turbomachinery flows // Proceedings of the 2nd European Conference on Turbomachinery Fluid Dynamics and Thermodynamics. Antwerpen, Belgium, March 5–7 1997. 99–108.

*Colonna P., Harinck J., Rebay S., Guardone A.* Real-Gas Effects in Organic Rankine Cycle Turbine Nozzles // Journal of Propulsion and Power. 2008. 24. 282–294.

*Hanimann Lucian, Mangani Luca, Casartelli Ernesto, Vogt Damian M., Darwish Marwan.* Real Gas Models in Coupled Algorithms Numerical Recipes and Thermophysical Relations // International Journal of Turbomachinery, Propulsion and Power. 2020. 5, 3.
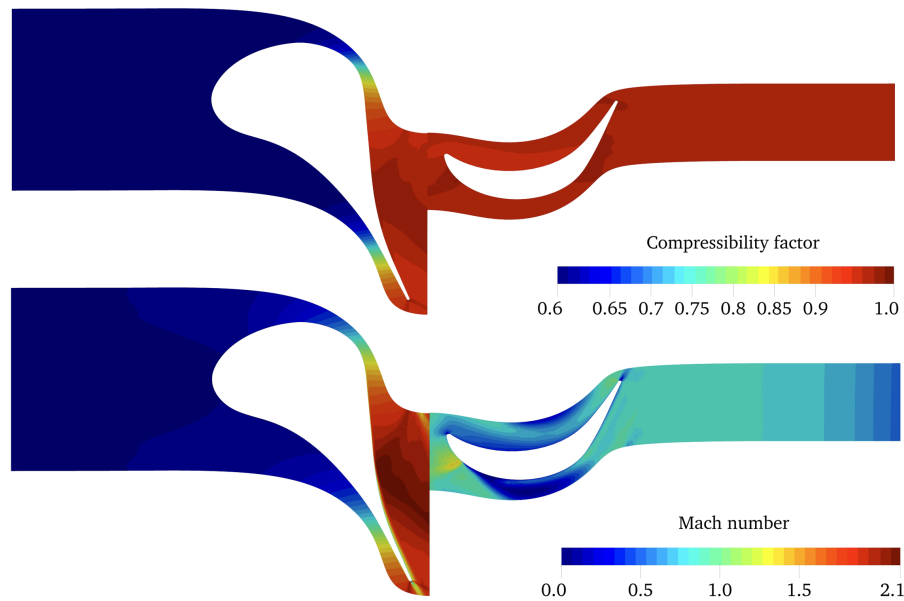
Figure 5: ORC turbine. Mach number contours (top) and compressibility factor at mid span (bottom) of the $1^{st}$-stage. $\mathbb{P}^2$ solution approximation and PR EoS. Distorted geometries: blade design is confidential property of the manufacturer.

*Peng D., Robinson D.* A New Two-Constant Equation of State // Industrial & Engineering Chemistry Fundamentals. 1976. 15, 1. 59–64.

*Pini M., Vitale S., Colonna P., Gori G., Guardone A., Economon T., Alonso J.J., Palacios F.* SU2: the Open-Source Software for Non-ideal Compressible Flows // Journal of Physics: Conference Series. mar 2017. 821, 1. 012013.

*Poling B.E., Prausnitz J.M., O'Connell J.P.* The Properties of Gases and Liquids 5E. 8787 Orion Place Columbus, OH 43240, USA: McGraw-Hill Education, 2000.

*Reynolds W.C.* Thermodynamic properties in SI: Graphs, tables, and computational equations for forty substances. Department of Mechanical Engineering: Stanford University, 1979.

*Roe P.L.* Approximate Riemann solvers, parameter vectors, and difference schemes // Journal of Computational Physics. 1981. 43, 2. 357–372.

*Saxer A.P., Giles M.B.* Quasi-three-dimensional nonreflecting boundary conditions for Euler equations calculations // Journal of Propulsion and Power. 1993. 9, 2. 263–271.

*Vinokur M., Montagné J.* Generalized flux-vector splitting and Roe average for an equilibrium real gas // Journal of Computational Physics. 1990. 89, 2. 276–300.